

Original

Vicen-Bueno, R.; Horstmann, J.; Terril, E.; de Paolo, T.; Dannenberg, J. :
**Real-Time Ocean Wind Vector Retrieval from Marine Radar
Image Sequences Acquired at Grazing Angle**

In: Journal of Atmospheric and Oceanic Technology (2013) AMS

DOI: 10.1175/JTECH-D-12-00027.1

Real-Time Ocean Wind Vector Retrieval from Marine Radar Image Sequences Acquired at Grazing Angle

RAUL VICEN-BUENO

University of Alcala, Alcala de Henares, Madrid, Spain

JOCHEN HORSTMANN

NATO Undersea Research Center, La Spezia, Italy, and Institute of Coastal Research, Helmholtz-Zentrum Geesthacht, Hamburg, Germany

ERIC TERRIL AND TONY DE PAOLO

Coastal Observing Research and Development Center, Scripps Institution of Oceanography, La Jolla, California

JENS DANNENBERG

OceanWaveS GmbH, Luneburg, Hamburg, Germany

(Manuscript received 15 February 2012, in final form 23 July 2012)

ABSTRACT

This paper proposes a novel algorithm for retrieving the ocean wind vector from marine radar image sequences in real time. It is presented as an alternative to mitigate anemometer problems, such as blockage, shadowing, and turbulence. Since wind modifies the sea surface, the proposed algorithm is based on the dependence of the sea surface backscatter on wind direction and speed. This algorithm retrieves the wind vector using radar measurements in the range of 200–1500 m. Wind directions are retrieved from radar images integrated over time and smoothed (averaged) in space by searching for the maximum radar cross section in azimuth as the radar cross section is largest for upwind directions. Wind speeds are retrieved by an empirical third-order polynomial geophysical model function (GMF), which depends on the range distance in the upwind direction to a preselected intensity level and the intensity level. This GMF is approximated from a dataset of collocated in situ wind speed and radar measurements ($\sim 31\,000$ measurements, ~ 56 h). The algorithm is validated utilizing wind and radar measurements acquired on the Research Platform (R/P) *FLIP* (for *Floating Instrumentation Platform*) during the 13-day Office of Naval Research experiment on High-Resolution Air–Sea Interaction (HiRes) in June 2010. Wind speeds ranged from 4 to 22 m s^{-1} . Once the proposed algorithm is tuned, standard deviations and biases of 14° and -1° for wind directions and of 0.8 and -0.1 m s^{-1} for wind speeds are observed, respectively. Additional studies of uncertainty and error of the retrieved wind speed are also reported.

1. Introduction

The energy exchange between atmosphere and ocean is one of the major processes driving ocean and atmospheric dynamics. When studying these processes, one of the most important parameters to measure is the wind. Several in situ and remote methodologies exist to measure

ocean winds. Wind measurements are usually obtained in situ, for example by cup or ultrasonic anemometers. However, these measurements are sometimes affected by the installation on the platform (blockage or shadowing) and/or local turbulence, resulting in inaccurate wind measurements. Within this paper, we introduce a real-time methodology based on marine radars for measuring the dominant wind vector over a circular area of 4 km of radius (referred to as “wind vector” from here on). The radar is usually placed on the top of the mast of moving platforms, as occur in our case of study. In this way, the radar is usually exempt of blockage and

Corresponding author address: Raul Vicen-Bueno, Signal Theory and Communications Department, University of Alcala, Ctra. Madrid-Barcelona km 33.1, 28805, Alcala de Henares, Madrid, Spain.
E-mail: raul.vicen@uah.es

shadowing and most of the time is out of the turbulence. In these situations, the radar-based method proposed in this paper is presented as an alternative or complement to anemometers. In addition, this proposal is useful and cheaper than anemometers when a radar is already installed on the platform. Otherwise, the anemometer is a cheaper and simpler piece of equipment.

Marine radars operate in the X band (9.5 GHz) under grazing incidence. The backscatter of the ocean surface is primarily caused by the small-scale surface roughness (~ 3 cm), which in turn is strongly dependent on the local wind speed (Chaudhry and Moore 1984; Lee et al. 1995; Trizna 1997) and wind direction (Trizna and Carlson 1996). For wind speeds stronger than $\sim 15 \text{ m s}^{-1}$, the small-scale roughness of ~ 3 cm is not dominant because of longer steep wind waves, whitecapping, and breaking. In this case, the “Bragg” mechanism is usually considered as a classic approach. It is known that, in the presence of long surface waves (swell), the small-scale surface roughness (wind waves), and consequently the radar backscatter, is modulated, which leads to the imaging of surface waves. In the past, marine radar image sequences have been operationally used to determine two-dimensional wave spectra (Young et al. 1985) and significant wave height (Nieto-Borge et al. 2004). Furthermore, marine radars have been used to measure near-surface currents (Senet et al. 2001; Trizna 2010), bathymetry (Bell 1999; Flampouris et al. 2008), individual waves (Dankert and Rosenthal 2004), and wave groups (Dankert et al. 2003a) and to detect ships (Vicen-Bueno et al. 2011a). Marine radars are also useful for estimating wind speed and direction (Dankert et al. 2003b; Dankert and Horstmann 2007). In these two works, wind directions were extracted from wind-induced streaks, which are visible in radar images integrated over time. Up to the present, the source of the wind-induced streaks visible in radar images has been under discussion. The most likely sources are the Langmuir circulation structure, a feature of the wave- and wind-driven turbulence of the upper ocean (McWilliams et al. 1997), as well as the airflow of turbulent eddies at the boundary layer (Drobinski and Foster 2003). With this wind streak-based methodology, the wind direction is retrieved with a 180° directional ambiguity and a standard deviation of 13° with a negligible bias of -1° . However, the methodology is only applicable to static platforms. Because of the motion of the platform, the wind-induced streaks, in particular if they are oriented perpendicular to the platform heading, will be reduced or even removed because of the temporal averaging process required to remove the ocean waves. The motion of the platform will significantly reduce the accuracy of wind direction estimates. In addition, the wind direction ambiguity removal process used in their

algorithm does not work for moving platforms. The wind speed retrieval in Dankert et al. (2003b) and Dankert and Horstmann (2007) results from the dependency of the radar cross section (RCS) on wind direction, wind speed, and range distance to the radar. This dependency is described by an empirical geophysical model function (GMF), which has to be estimated for each individual system, since marine radar systems are not radiometrically calibrated. Comparison to in situ wind speed measurements results in a standard deviation of 0.9 m s^{-1} with no bias. Unfortunately, the calibration/tuning stage for estimating the empirical GMF requires a large dataset with collocated radar and wind measurements (~ 160 h, or ~ 6.5 days, were needed in these studies for this stage), and it must include the full range of wind speeds that are anticipated.

To overcome the limitations mentioned above, our methodology has to be independent of the platform movement and has to be easily adjustable to other radars and radar setups with the least possible calibration effort. Furthermore, the proposed solution should solve the typical problems of anemometers installed on large platforms, including blockage, shadowing, and turbulence. Last but not least, the algorithm has to work in real time.

The paper is organized into five sections. Section 2 describes the instrumentation and data used in this study. Section 3 introduces the algorithm for retrieving the wind direction and speed from marine radar image sequences. Section 4 presents the results of the wind vector retrieval algorithm compared to actual wind vector measurements. These results are presented for the design stage and validated with another dataset collected in the same experiments. Furthermore, this section presents a study of the uncertainty of the retrieved wind speed and a study of the limits of the errors that can be expected during the wind speed retrieval process, as well as a real-time applicability study. Finally, in section 5 we draw the main conclusions and propose future research on this topic.

2. Instrumentation and data used in the experiments

The data utilized for the design and validation of the marine radar-based wind vector retrieval algorithm proposed in this paper were acquired during the Office of Naval Research experiment on High-Resolution Air–Sea Interaction (HiRes). This experiment was carried out in June 2010, approximately 30 km northwest of Bodega Bay, California. The radar and wind data were collected from the Research Platform (R/P) *FLIP* (for *Floating Instrumentation Platform*). An ultrasonic

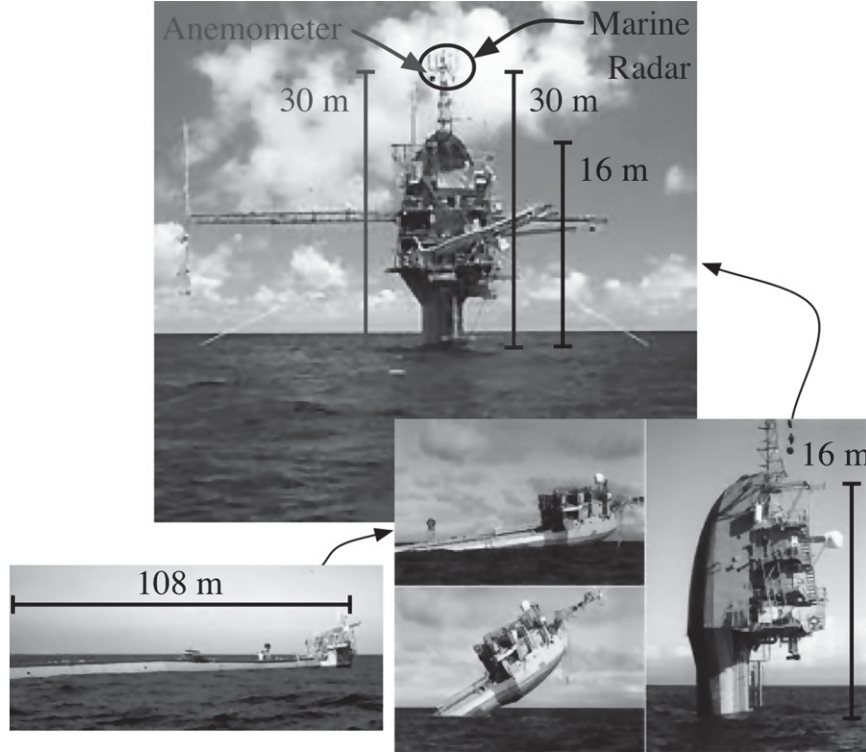


FIG. 1. Research platform (R/P) *FLIP* during the setup stage for the High-Resolution Air-Sea Interaction (HiRes) experiment carried out in June 2010. The sensors used in the experiment and their installation heights are highlighted.

anemometer and a marine radar, both installed at a height of 30 m above mean sea level, were used. Figure 1 shows the R/P *FLIP* during the setup stage, including the locations of the sensors and their installation heights.

During the HiRes experiment, anemometer and marine radar data were collected from 7 to 19 June 2010 during four periods:

- Period 1: from 00:57:24 7 June to 07:07:25 9 June 2010;
- Period 2: from 15:21:44 9 June to 20:58:21 12 June 2010;
- Period 3: from 19:31:00 13 June to 16:04:16 14 June 2010;
- Period 4: from 15:20:04 16 June to 11:47:16 19 June 2010.

During the experiment, strong northwesterly winds ($\sim 320^\circ$ and $\sim 16 \text{ m s}^{-1}$) predominated. Wind sea and no swell were generally experienced. The wind data from the ultrasonic anemometer were collected at a rate of 10 measurements per minute. The wind measurements were converted to a 10-min running average, with resulting wind speeds ranging from 4 to 22 m s^{-1} . Time plots of the wind data measured by the anemometer are presented in Fig. 2. The wind measurements were

obtained by carefully avoiding blockage and shadowing when locating the anemometer.

The marine radar utilized in this experiment is a standard off-the-shelf marine radar (Furuno 2117BB), which operates at 9.5 GHz (X band) in horizontal polarization in transmit and receive with an output power of 12 kW. The radar was operated in short pulses (50 ns) with a pulse repetition frequency (PRF) of 1600 Hz. The radar was equipped with an 8-ft antenna that was rotating at a speed of 40 rpm (one radar image every 1.5 s). The radar covers 360° in azimuth, with an azimuthal resolution of 0.15° , and has a range coverage of $\sim 3950 \text{ m}$ (starting at 120 m in the near range), with a range resolution of 7.5 m. The marine radar was connected to an analog-to-digital (AD) converter. This AD converter is incorporated in the Wave Monitoring System II (WaMoS II). This system digitizes the radar backscatter measured for each azimuth-range cell, forming a digital radar image. The digital images are saved into a standard personal computer using a 12-bit unsigned integer format, with each cell having a dynamic range of [0, 4095]. The radar was placed on the top of the mast. Therefore, blockage and shadowing are completely avoided in the radar measurements. Nevertheless, neither the anemometer nor the radar is exempt of turbulence effects. However, these

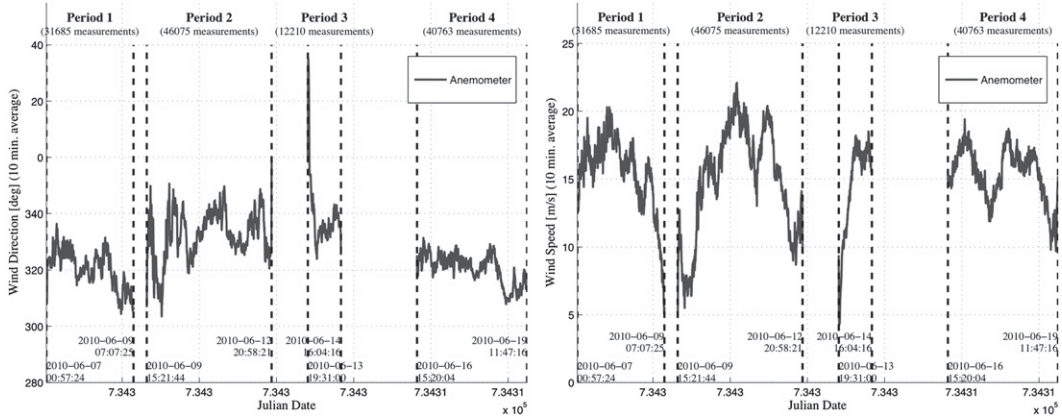


FIG. 2. Time series (10-min average) of (left) wind direction and (right) wind speed measurements acquired by the anemometer at 30-m height during four periods of the HiRes experiment.

effects were of small magnitude during the measurement campaign.

Figure 3 shows two examples of radar images, which were acquired at wind speeds of 5 and 15 m s⁻¹. The radar operates up to 3952.5 m. But since the radar intensity is proportional to the range (R) as $1/R^4$, and the range resolution depends on the local incident angle, which changes with the distance, the radar images are plotted up to 1500 m to illustrate better the details of interest within this study. All radar images are oriented north, and the corresponding wind direction given by the anemometer is depicted within each radar image by the bar in the center of the image.

3. Marine radar image sequence-based wind vector retrieval algorithm

Analyzing the radar images obtained during the experiment, we observe an increase in mean image intensity

(radar backscatter) with increasing wind speed. In addition, we observe a strong image intensity dependence on wind direction, resulting in larger intensities for the upwind direction than for the crosswind and downwind directions. These dependencies were also observed by Trizna (1997), Dankert et al. (2003b), and Dankert and Horstmann (2007), which can be seen in the marine radar images depicted in Fig. 3. These dependencies on wind direction and speed are the basis of the algorithm proposed in this paper. This algorithm consists of three steps, which are summarized in Fig. 4. In the first step, radar images are integrated over time and smoothed in space. Temporal integration is applied to remove all signatures due to ocean waves. Space smoothing reduces the variance of the intensity of the integrated radar image due to speckle. In this way, better estimates of the direction and radius (lately converted to speed) for the upwind peak are made. In the second step, wind directions are retrieved by searching for the upwind peak in the integrated

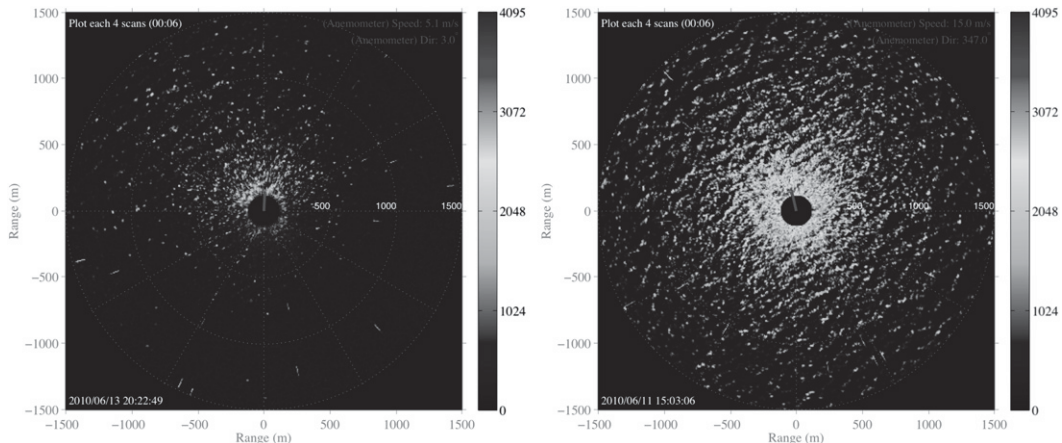


FIG. 3. Example of radar images for wind speeds and directions of (left) 5 m s⁻¹ and 3° and (right) 15 m s⁻¹ and 347°.

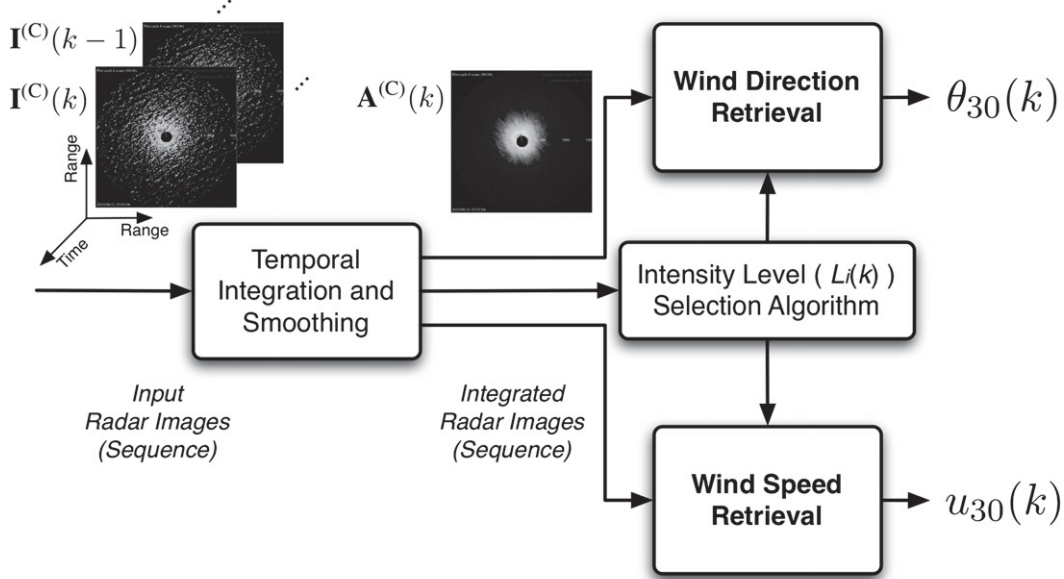


FIG. 4. Block diagram of the proposed algorithm for retrieving the wind direction and speed from marine radar image sequences.

and smoothed radar images. Finally, in the third step, wind speeds are retrieved by measuring the maximum range distance to a preselected intensity value. This maximum range distance is empirically demonstrated to be related to the wind speed.

In the following, we denote the radar image at a certain time instant, $t = kT_a$, as $\mathbf{I}(k)$, where T_a denotes the antenna rotation period ($T_a = 1.5$ s per image). The radar image at a previous ($n > 0$) or posterior ($n < 0$) time instant, $t = kT_a - nT_a$, is denoted as $\mathbf{I}(k-n)$. The integrated (and smoothed) radar image at the time instant $t = kT_a$ is denoted as $\mathbf{A}(k)$. The superindexes (P) or (C) indicate if the radar data matrices are in polar or Cartesian coordinates, respectively. A polar data format represents the data given by range–azimuth coordinates, which is the output of the WaMoS II AD converter (2400 azimuth and 512 range bins). A Cartesian data format represents the data given by X – Y range coordinates. Following the works of Vicen-Bueno et al. (2011b, 2009), we convert polar coordinates to Cartesian by averaging overlapping cells (in the near range) and linearly interpolating cells with no collocated values (in the far range).

a. Temporal integration and smoothing of marine radar images

The temporal integration is performed by utilizing a moving average of N radar images with a shift of four images (sliding window). The shift of four images (6 s) was selected in accordance with the frequency of available

wind measurements (10 measurements per minute). The integration and smoothing of the radar data are performed in polar coordinates [$\mathbf{I}^{(P)}$] by the following steps:

- (i) Integration of N input radar images (size 2400×512):

$$\mathbf{A}^{(P)}(k) = \frac{1}{N} \sum_{n=0}^{N-1} \mathbf{I}^{(P)}(k-n). \quad (1)$$

- (ii) Smoothing of each element (p, q) of the integrated radar image in the range direction, in which the two leading and two lagging range cells are considered:

$$\begin{aligned} A_{p,q}^{(P)}(k) = & \frac{1}{5} [A_{p,q-2}^{(P)}(k) + A_{p,q-1}^{(P)}(k) + A_{p,q}^{(P)}(k) \\ & + A_{p,q+1}^{(P)}(k) + A_{p,q+2}^{(P)}(k)], \\ p = 1, 2, \dots, 2400, \end{aligned} \quad (2)$$

where q varies from 3 to 510. For $q = [1, 2, 511, 512]$, $A_{p,q}^{(P)}(k) = A_{p,q}^{(P)}(k)$ (i.e., no smoothing is done). In this study, averaging is selected as smoothing technique, although other smoothing techniques could be considered, such as the median filter.

The additional smoothing is incorporated to reduce the noise in range direction. This noise reduction makes more accurate and stable the wind speed retrieval algorithm based on range measurements, as will be discussed in section 3c.

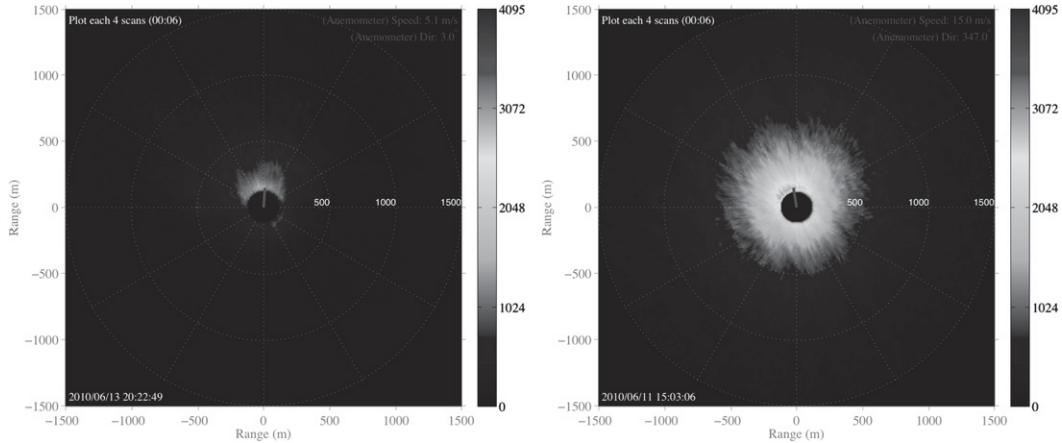


FIG. 5. Example of integrated radar images for different wind speeds (and directions) when using 64 radar images for integrating over time: (left) 5 m s^{-1} and 3° and (right) 15 m s^{-1} and 347° .

We have investigated the impact of N on the wind retrieval algorithm for values of 16, 32, 64, and 128. For small values of N , such as 16 and 32, ocean wave information is still present in the integrated radar images, which results in noisy wind estimates. In case of large values of N , such as 128, the intensity pattern in the integrated radar image is more stable and better defined than for low values of N . However, changes in wind direction and speed are observed with a delay, and short-term wind fluctuations cannot be detected. Comparison to 10-min average winds has shown that utilizing 64 radar images (corresponding to ~ 96 s) is a good compromise. Two examples of integration and smoothing using $N = 64$ radar images are plotted in Fig. 5. These examples represent the same times and range distances as for the radar images depicted in Fig. 3. The ocean waves, which were visible in Fig. 3, have been averaged out. The only information left in both images is an azimuth-dependent intensity pattern with a larger radar cross section in the upwind direction. Furthermore, there is a clear mean image intensity increase when the image is acquired at 15 m s^{-1} (Fig. 5, right side).

b. Wind direction retrieval stage

As observed in Fig. 5, the radar cross section at a given image intensity level is largest in the upwind direction. This behavior will be the basis of the wind direction retrieval stage. This upwind peak of the radar cross section is found in the integrated and smoothed radar image $\mathbf{A}^{(P)}(k)$ by the following steps:

- Select a certain image intensity level $[L_i(k)]$ from a set of predefined levels (L_1, L_2, \dots). The value $L_i(k)$ will be automatically selected by a procedure described at the end of this section. The range of

intensity levels is dependent on the radar system and radar setup and has to be selected in accordance. In our case, by analyzing the histograms of integrated radar images for low and high wind speeds, minimum and maximum intensity levels of 100 and 2000 were found, respectively. The predefined levels set in our study were $L_1 = 100, L_2 = 200, \dots, L_{20} = 2000$.

- Measure for each azimuthal direction p (from 0° : index $p = 1$, to 359.85° : index $p = 2400$) the maximum range distance where the intensity is equal to or greater than the selected intensity level $L_i(k)$. This range distance is stored in the p th element of the range distances vector for $L_i(k)$ [$\mathbf{r}_i(k)$]; that is,

$$r_{i,p}(k) = 120 + 7.5 \times (h - 1),$$

$$h \text{ index for first } \{A_{p,q}^{(P)}(k) \geq L_i(k), q = 1, 2, \dots, 512\}, \quad (3)$$

where 120 m is the near range distance boundary of the radar coverage.

- Smooth $\mathbf{r}_i(k)$ in the azimuthal direction to get a less noisy vector. This smoothing consists of averaging the range distances within a sector of 5° (~ 33 azimuthal directions); that is,

$$r_{i,p}^S(k) = \frac{1}{33} \sum_{q=p-16}^{p+16} r_{i,q}^E(k), \quad p = 1, 2, \dots, 2400, \quad (4)$$

where $\mathbf{r}_i^E(k)$ is the extended version of the vector $\mathbf{r}_i(k)$, being given by

$$\mathbf{r}_i^E(k) = [\mathbf{r}_i^{S,\text{End}}(k) \mathbf{r}_i^S(k) \mathbf{r}_i^{S,\text{Begin}}(k)]. \quad (5)$$

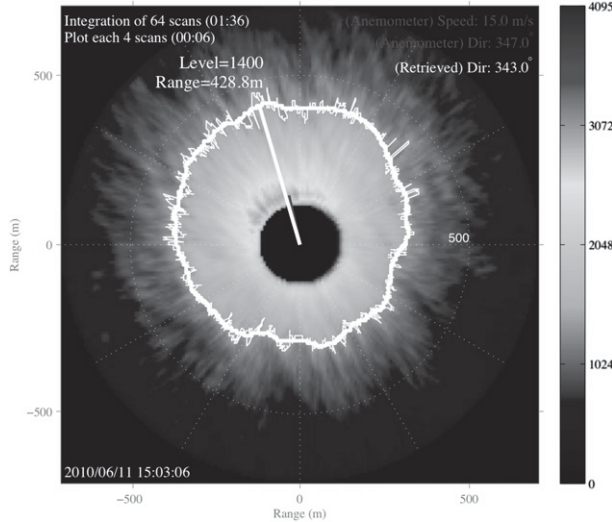


FIG. 6. Example of application of the wind direction retrieval stage of the proposed algorithm when using the integrated radar image of Fig. 5 (right) for a wind speed of 15 m s^{-1} .

This extended vector avoids the smoothing problem at the beginning (0° : index 1) and ending (359.85° : index 2400) boundaries of $\mathbf{r}_i(k)$. The vector $\mathbf{r}_i^{S,\text{End}}(k)$ contains the last 16 elements of $\mathbf{r}_i^S(k-1)$ (previous integrated radar image) and the vector $\mathbf{r}_i^{S,\text{Begin}}(k)$ should contain the first 16 elements of $\mathbf{r}_i^S(k+1)$ (next integrated radar image). But since we want the proposed algorithm to work in real time, the vector $\mathbf{r}_i^{S,\text{Begin}}(k)$ contains the first 16 elements of $\mathbf{r}_i^S(k)$ (current integrated radar image).

(iv) Finally, search for the position of the maximum range distance in $\mathbf{r}_i^S(k)$. The azimuth angle corresponding to this position is the wind direction; that is,

$$\begin{aligned}\theta_{30}(k) &= 0.15^\circ \times (a-1), \\ a &= p \quad \text{when} \quad r_{i,p}^S(k) = \max\{\mathbf{r}_i^S(k)\}, \\ p &= 1, 2, \dots, 2400.\end{aligned}\quad (6)$$

An example of how the proposed algorithm retrieves the wind direction from the integrated radar image of Fig. 5 (wind speed: 15 m s^{-1}) is presented in Fig. 6. For a better visualization, the range distance was limited to 700 m. For this example, an intensity level of 1400 was selected (step 1). The vector of range distances for $L_{14} = 1400$ [$\mathbf{r}_{14}(k)$ from step 2] and its smoothed version [$\mathbf{r}_{14}^S(k)$ from step 3] are plotted in Fig. 6 by solid thin and solid bold white lines, respectively. The azimuthal direction at which the maximum range distance is depicted (step 4) is plotted by the white wind direction bar with the origin in the center of the radar image. The retrieved and in situ

measured wind directions are similar, 343° and 347° , respectively.

As the level of intensity in the radar images changes depending on the wind speed, the intensity value L_i in the above-described wind direction retrieval stage has to be selected accordingly. Therefore, an adaptive algorithm is used to select $L_i(k)$, which operates as follows:

- At the start of the $L_i(k)$ selection algorithm (first 16 iterations), all the predefined intensity levels (L_1, L_2, \dots, L_{20}) are considered in each iteration. All the smoothed range distance vectors $[\mathbf{r}_i^S(k), i = 1, 2, \dots, 20]$ are computed in each iteration. From these vectors, the one with the lowest L_i for which all its elements are greater than the near-range distance boundary plus a guard range ($120 \text{ m} + 80 \text{ m} = 200 \text{ m}$) is selected.
- After the first 16 iterations, only the last selected level $[L_i(k-1)]$ and its upper $[L_{i+1}(k-1)]$ and lower $[L_{i-1}(k-1)]$ intensity levels are considered in the wind direction retrieval stage. From the three smoothed range distance vectors $[\mathbf{r}_{i-1}^S(k-1), \mathbf{r}_i^S(k-1), \text{ and } \mathbf{r}_{i+1}^S(k-1)]$, the one fulfilling the same constraint used in the startup and with the lowest intensity level is selected. To speed up the algorithm, only three intensity levels are used to estimate the wind speed. With these three levels, we ensure that the algorithm is able to adapt to the fastest wind speed changes observed in the experiments.

Finally, it is important to note that during the running of the $L_i(k)$ selection algorithm, when a wind speed decrease is observed, an automatic decrease of the selected level is applied, and vice versa. In this way, the algorithm is stable and automatically adapts to wind speed changes.

c. Wind speed retrieval stage

The integrated and smoothed radar images obtained in the experiments (see Fig. 5 as an example) show that the wind speed can be related to the maximum range at which a certain intensity level $L_i(k)$ is reached [$\max\{\mathbf{r}_i^S(k)\}$]. The conversion from measured range to wind speed (at 30-m height) proposed in this paper can be done by

$$u_{30}(k) = f[L_i(k), \max\{\mathbf{r}_i^S(k)\}], \quad (7)$$

where $L_i(k)$ and $\mathbf{r}_i^S(k)$ are obtained from the wind direction retrieval stage (see section 3b).

The conversion function proposed in Eq. (7) is divided into two steps. First, the conversion rate (α_i) is chosen according to the selected intensity level (L_i), as defined in Eq. (8). Second, the conversion from range distance to

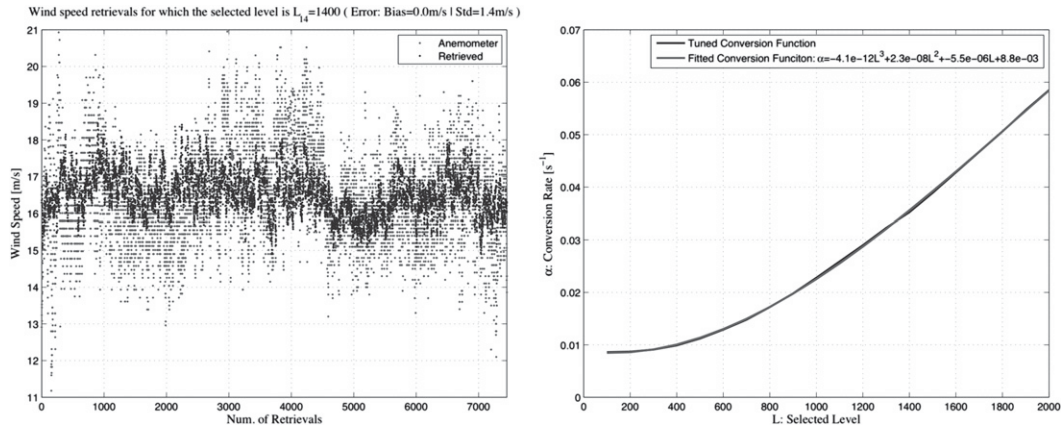


FIG. 7. Example of tuning of the conversion rate (α) for an intensity level of $L_{14} = 1400$ and the achieved tuned (discrete version) and fitted (continuous version) conversion functions. (left) Maximum ranges from 423.3 to 524.1 m and $\alpha_{14} = 0.0354 \text{ s}^{-1}$; retrieved wind speeds from 15.0 to 18.6 m s^{-1} . (right) Tuned (discrete) and fitted (continuous) versions of the conversion function $g()$.

wind speed is done according to the selected conversion rate (α_i), as set in Eq. (9):

$$\alpha_i(k)[\text{s}^{-1}] = g[L_i(k)], \quad (8)$$

$$u_{30}(k)[\text{m s}^{-1}] = \alpha_i(k) \times \max\{\mathbf{r}_i^S(k)\}. \quad (9)$$

To have an idea of the magnitude of the conversion rates, consider the example in Fig. 6. In this case, an intensity level of $L_{14} = 1400$ was used, obtaining $\max\{\mathbf{r}_{14}^S(k)\} = 428.8 \text{ m}$. Therefore, from Eq. (9), this wind speed (15 m s^{-1}) requires a conversion rate of $\alpha_{14} = 15.0 \text{ m s}^{-1}/428.8 \text{ m} = 0.0349 \text{ s}^{-1}$ for a correct $u_{30}(k)$ estimate. The procedure to obtain $g()$ is complex. It is made in the design stage, where the in situ anemometer measurements and marine radar data of period 1 of the database (see section 2) are used. This procedure is divided into three steps:

- (i) Obtain the measurements of the maximum range distance [$\max\{\mathbf{r}_i^S(k)\}$] for each integrated radar image of the design dataset ($k = 1, 2, \dots, M_{\text{design}}$), considering the adaptive algorithm used to select $L_i(k)$ for each radar image k . These measurements are taken every four images (temporal integration shift; i.e., every 6 s in our case of study).
- (ii) Select the measurements of the maximum range distance that were achieved for the first intensity level under study, that is for $L_1 = 100$. Calculate the conversion rate (α_1) that minimizes the mean of the wind speed retrieval error for the measurements related to L_1 .
- (iii) Repeat step 2 for the remaining intensity levels under study, that is for $L_2 = 200, \dots, L_{20} = 2000$.

Then, all the conversion rates are found ($\alpha_2, \dots, \alpha_{20}$) and a discrete version of the nonlinear conversion function, $g()$, is obtained.

In our case of study, applying step 1, $M_{\text{design}} = 31\,685$ measurements are obtained from the design dataset (period 1). From all these measurements, as an example, consider an intensity level of $L_{14} = 1400$, which is typical for retrieving medium to high wind speeds. Applying step 2, 7298 values are found for L_{14} , obtaining a conversion rate of $\alpha_{14} = 0.0354 \text{ s}^{-1}$. According to this conversion rate and to the maximum range distances achieved from these measurements ($\in [423.3, 524.1] \text{ m}$), wind speeds in the range of $[15.0, 18.6] \text{ m s}^{-1}$ are retrieved. The wind speeds from the anemometer and retrieved by the proposed algorithm are depicted in Fig. 7 (left) for the measurements with an intensity level of L_{14} . Finally, applying step 3 for calculating the conversion rates for the other intensity levels ($L_i = i \times 100, i = 1, 2, \dots, 20, i \neq 14$), the discrete (tuned) conversion function depicted in Fig. 7 (right) is obtained. This conversion function (discrete) is nonlinear and can be fitted by a third-order polynomial continuous function:

$$\alpha = \beta_3 L^3 + \beta_2 L^2 + \beta_1 L + \beta_0. \quad (10)$$

The parameters of this function can be found by using the total least squares algorithm of Golub and Van Loan (1980), being in our case of study $\beta_3 = -4.1 \times 10^{-12}$, $\beta_2 = 2.3 \times 10^{-8}$, $\beta_1 = -5.5 \times 10^{-6}$, and $\beta_0 = 8.8 \times 10^{-3}$. Figure 7 also shows the resulting continuous conversion function. The results presented in section 4 for the design

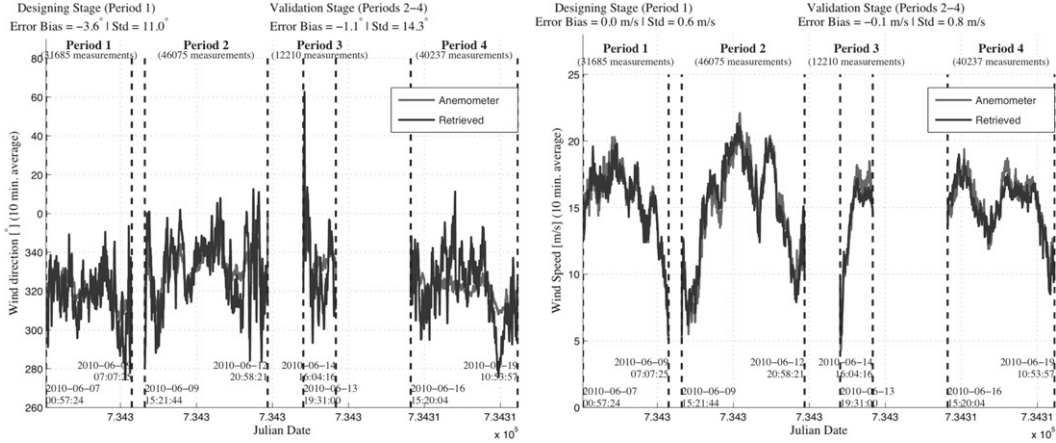


FIG. 8. Comparison of the (left) wind directions and (right) wind speeds given by the anemometer and retrieved by the proposed wind vector retrieval algorithm for the design (period 1) and validation (periods 2–4) datasets.

and test stages are obtained using this nonlinear continuous conversion function.

4. Experimental results

Once the wind vector retrieval algorithm is tuned [N is set in the integration stage, no tuning is needed in the wind direction retrieval stage, and the nonlinear conversion function of Eqs. (7)–(9) is calculated in the wind speed retrieval stage], four main questions can be asked:

- (i) Is the algorithm performance in the design stage maintained for a different dataset of radar images? This question is discussed in section 4a.
- (ii) Once the algorithm is designed and validated, what is the uncertainty of the retrieved wind speeds? This question is answered from two different approaches in section 4b.
- (iii) How robust is the proposed algorithm with range distance measurement errors? This question is studied in section 4c.
- (iv) Can this algorithm work in real time? This question is analyzed in section 4d.

a. Performance evaluation of the wind vector retrieval algorithm in the design and validation stages

The performance of the proposed algorithm when retrieving the wind vector (direction and speed) from marine radar image sequences is depicted in Fig. 8. The performance for the whole database (periods 1–4 in section 2) is depicted. The database is divided into two datasets: the design dataset (period 1) and the validation dataset (periods 2–4). As previously mentioned, the design dataset is used to tune the proposed algorithm. The validation dataset is used to analyze the performances for

a different dataset, helping to predict how the algorithm will perform in the future.

Starting with the analysis of the results obtained when retrieving the wind direction (see Fig. 8), different performance results are obtained in each stage. For the design dataset, the bias and standard deviation of the wind direction retrieval errors are -3.6° and 11.0° , respectively. For the validation dataset, these error statistics are -1.1° and 14.3° , respectively. The statistics are similar, with the validation dataset being slightly greater. Moreover, these statistics are similar to the ones taken as references from Dankert et al. (2003b) and Dankert and Horstmann (2007) ($\sim -1^\circ$ and $\sim 13^\circ$, respectively).

For the results obtained in the wind speed retrieval stage (see Fig. 8), the algorithm performance was measured for each stage. For the design dataset, the bias and standard deviation of the wind speed retrieval error are 0.0 and 0.6 m s^{-1} , respectively. Note that a null bias of the error is achieved, as expected from the tuning of the nonlinear conversion function described in section 4c. For the validation dataset, the bias and standard deviation of the wind speed retrieval error are -0.1 and 0.8 m s^{-1} , respectively. These statistics are slightly poorer than for the design stage, but they are still better (standard deviation) than the ones taken as reference in our studies from Dankert et al. (2003b) and Dankert and Horstmann (2007) (0.0 and 0.9 m s^{-1} , respectively). This low error increase (from design to validation) shows the robustness of the wind speed retrieval algorithm with changing wind conditions.

b. Uncertainty study of the retrieved wind speed

The previous subsection discussed how the performance of the proposed algorithm is practically maintained for a different dataset, but no discussion of the

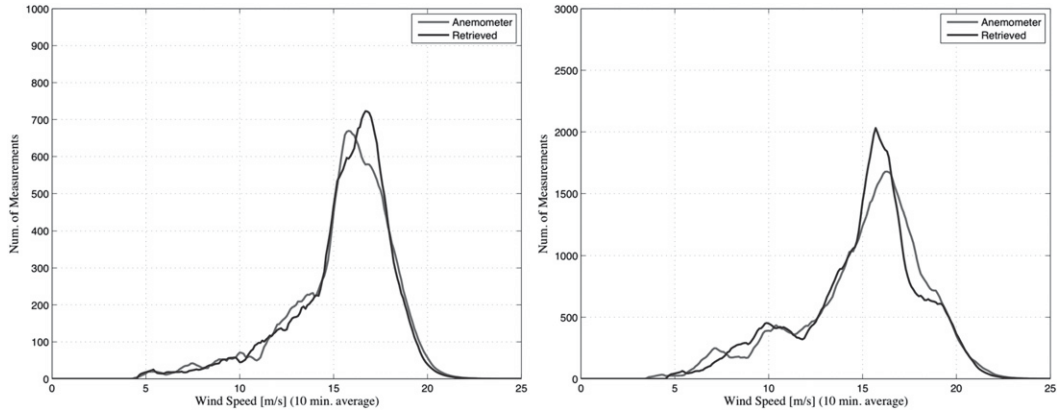


FIG. 9. Histograms of the wind speed measured by the anemometer and retrieved by the proposed algorithm for the periods of data relating to the (left) design (period 1) and (right) validation (periods 2–4) stages.

uncertainty of the retrieved information was given. In this subsection, the uncertainty associated with the retrieved wind speed is studied. This study is made by the analysis of the statistics of the wind speed retrieval error depending on the retrieved wind speed from two different, but related, approaches.

In the first approach, the histograms of the wind speed measured by the anemometer and retrieved by the proposed algorithm are compared for both the design and validation datasets (see Fig. 9). The design dataset histograms are similar, although some differences are found because of the error in the retrieval process. The uncertainty of the retrieved wind speed is expected to be equally distributed with the wind speed, being slightly higher in the range of $[15, 19] \text{ m s}^{-1}$. For the validation dataset, similar conclusions are drawn.

In the second approach, we set an objective measurement of the error associated with the retrieved wind speed using a box-and-whisker plot (Brase and Brase 2009) to analyze the wind speed retrievals and their errors. The box given for each wind speed ($5, 6, \dots, 21 \text{ m s}^{-1}$) has lines at the lower, median, and upper quartile values, where 25%, 50%, and 75% of data are lower than these values, respectively. Whiskers extend from each end of the box to the adjacent values in the data belonging to the most extreme values within 1.5 times the interquartile range (from lower to upper quartile values). The whiskers are plotted by dashed black lines. Outliers are data with values beyond the ends of the whiskers, which are displayed with a red plus sign. A solid red line plots the mean of the error for each wind speed. Next, the results for the design and validation datasets are analyzed by using this approach.

On the one hand, focusing on the analysis of the results for the design dataset (see Fig. 10), the mean error achieved for each wind speed is practically null. It is

practically null but not exactly null because the tuning of the nonlinear conversion function looks for a null mean error for each selected level and not a null mean error for each wind speed. Figure 10 also shows that the boxes have a height lower than $\pm 1 \text{ m s}^{-1}$ with respect to the median of each one. This result is similar to the standard deviation of the error achieved in Fig. 8 (0.6 m s^{-1}). The heights of the boxes and whiskers are small for low to medium wind speeds and high wind speeds, indicating low uncertainty for these retrieved wind speeds. However, these heights increase for medium wind speeds ($\in [15, 19] \text{ m s}^{-1}$), which was also observed when analyzing the histograms in Fig. 9. Finally, note that there are only a few outliers ($\sim 2\%$ of the retrievals), which are mainly localized for wind speeds greater than 12 m s^{-1} .

On the other hand, focusing on the analysis of the wind speed retrievals for the validation dataset (see Fig. 10), the wind speed uncertainty is similar to that found in the design dataset (mean and median errors close to zero, except for 5 m s^{-1} ; height of the boxes lower than $\pm 1 \text{ m s}^{-1}$; and a few outliers). Slightly larger boxes and whiskers are seen in the validation stage, endorsing the difference of the standard deviation of the error given in Fig. 8 for the design (0.6 m s^{-1}) and validation (0.8 m s^{-1}) stages.

c. Robustness of the wind speed retrieval algorithm stage with range distance measurement errors

This section presents the answers to the following questions: How robust is the proposed algorithm when errors in the wind speed retrieval stage are made? Can these errors be quantified?

To find the answers, we artificially provoke errors during the measurement of the range distance at which the maximum of the intensity pattern ($\max\{\mathbf{r}_i^S\}$) is given. These artificial errors occur during the retrieval of the wind speed in Eqs. (7)–(9). In this case, errors of $\pm 7.5 \text{ m}$

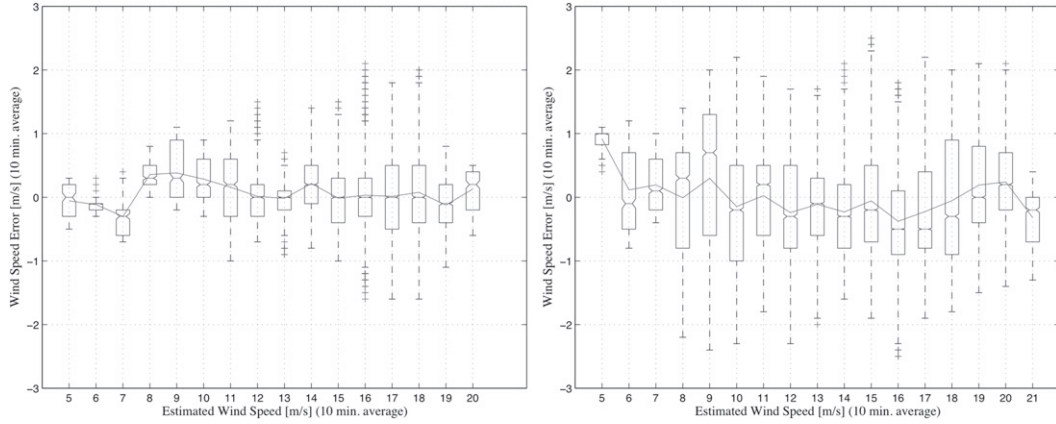


FIG. 10. Uncertainty (associated error) of the wind speed retrieved by the proposed algorithm for the periods of data relating to the (left) design (period 1) and (right) validation (periods 2–4) stages.

(probable error conditions) and ± 22.5 m (extreme error conditions) in the measurements of $\max\{\mathbf{r}_i^S\}$ are considered. Figure 11 shows the wind speeds retrieved when no artificial errors and artificial errors of ± 7.5 or ± 22.5 m are made. This figure only shows the results for a segment of the validation dataset, once the algorithm is tuned. This segment includes the first half of period 2, where wind speeds for practically the whole range ($[5, 22]$ m s $^{-1}$) are available. The bias and standard deviation of the wind speed retrieval error are given for the whole validation dataset. Results for the design dataset, which are not shown, are similar, but the error statistics are lower, as expected from the results presented in the previous sections.

There are three main findings from the results in Fig. 11:

- (i) The wind speed error increases with the error of $\max\{\mathbf{r}_i^S\}$.
- (ii) The standard deviation of the wind speed retrieval error is nearly constant, while the bias changes: ± 0.25 m s $^{-1}$ for a range distance error of ± 7.5 m, and ± 0.75 m s $^{-1}$ for a range distance error of ± 22.5 m. The bias increases linearly with the range distance error (an increase of 3 times in errors, including artificial errors).
- (iii) The error made for high wind speeds is greater than for low wind speeds. This can be seen with an artificial error of ± 22.5 m in $\max\{\mathbf{r}_i^S\}$ (see Fig. 11). This effect is because the conversion rates corresponding to high wind speeds (right part of the conversion function plotted in Fig. 7) are greater than for low wind speeds (left part of Fig. 7).

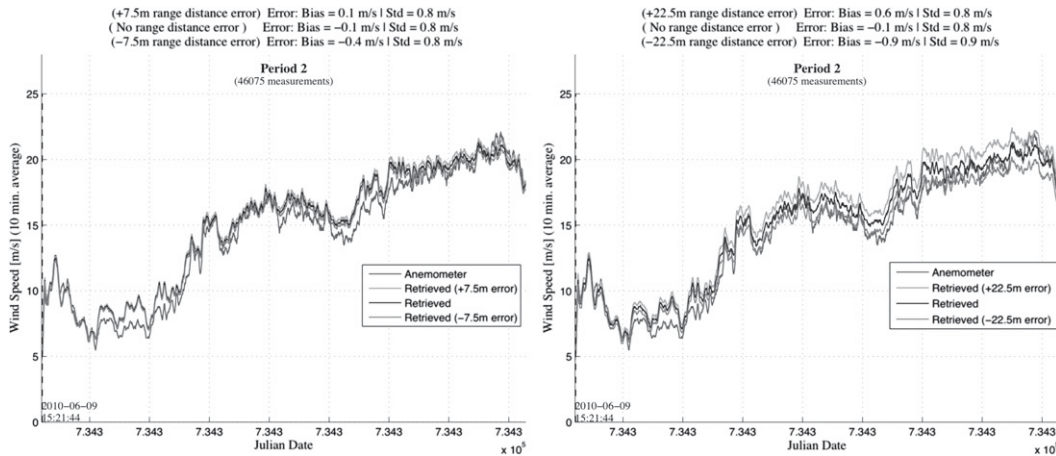


FIG. 11. Influence of artificial errors of (left) ± 7.5 or (right) ± 22.5 m in the measurement of the maximum range distance during the wind speed retrieval stage of the proposed algorithm. Analysis is for the first half of period 2 of the validation dataset.

In conclusion, the proposed algorithm is robust. Errors made in the wind speed retrieval stage have a low error bias and practically a null variation of the standard deviation. Thus, the error bias increase can be limited to $\pm 0.25 \text{ m s}^{-1}$ for the most probable error conditions.

d. Computation time of the proposed algorithm

A final step is to study the computational cost of the algorithm. For this study, a standard personal computer is used, running Linux (Ubuntu 10.04) and using a 2.4-GHz Intel Core2 Duo CPU and 4 GB of DDR2PC2-5300 RAM. The data were stored in a 2-GB hard disk connected to the personal computer by a FireWire 800 interface. The algorithm was developed in Matlab 2007b.

The time needed to retrieve the wind direction and speed by the processing of 64 radar images (sliding window length)—that is, $64 \times 1.5 = 96 \text{ s}$ of data—is approximately 4 s. Since a sliding window is used, each set of 64 radar images is processed each four radar images (sliding window shift)—that is, each $4 \times 1.5 = 6 \text{ s}$ —retrieving a new wind vector. Therefore, because of the processing time is lower than the time between wind vector retrievals, the algorithm can be used in real-time applications. Note that there are still 2 s of CPU processing time (33% of the time) available for running other research software utilities, such as the future applications discussed in the next section.

5. Conclusions and future work

A new algorithm for retrieving the wind vector from marine radar image sequences in real time has been proposed in this paper. The proposed algorithm is based on two principles. The first one focuses on the observed relationship between the wind direction and the direction of the maximum range of an intensity pattern formed in the integrated and smoothed radar images. The second one, which is a novel approach, focuses on the nonlinear relationship between the range distance at which this maximum is found and the wind speed.

From the results presented in the paper, six main conclusions can be drawn:

- (i) The performance of the proposed wind vector algorithm is nearly the same from the design stage to the validation stage. The algorithm performance in these stages is similar to, and in the case of wind speed retrieval even better than, the best solutions proposed in the literature by using marine radars. From the best results reported in the literature (see Dankert et al. 2003b; Dankert and Horstmann 2007), the following results (mean|standard deviation) are approximately achieved: $-1^\circ|13^\circ$ for the wind direction and $0.0 \text{ m s}^{-1}|0.9 \text{ m s}^{-1}$ for the wind

speed. For the proposed algorithm we get $-1^\circ|14^\circ$ for the wind direction and $-0.1 \text{ m s}^{-1}|0.8 \text{ m s}^{-1}$ for the wind speed.

- (ii) A nonlinear function is empirically found to relate the wind speed and the range distance at which the maximum of the intensity pattern is achieved. This nonlinear function can be approximated by a third-order function for this radar. The methodology presented in this paper for finding this novel nonlinear function allows us to tune this function when working with other marine radars.
- (iii) For wind speed retrieval, the uncertainty is low (less than $\pm 1 \text{ m s}^{-1}$) and is almost equally distributed with the wind speed.
- (iv) The error made in the wind speed retrieval stage can be limited to $\pm 0.25 \text{ m s}^{-1}$ based on the most probable error conditions.
- (v) The algorithm can be used in real time on a standard personal computer. This is the most important aspect of the proposed algorithm because the algorithms selected from the literature (Dankert et al. 2003b; Dankert and Horstmann 2007) do not work in real time.
- (vi) Problems commonly reported with anemometers, such as induced blockage, shadowing, and/or turbulence, can be mitigated by the proposed marine radar solution.

This research work is not finished with this paper. For example, since there is still free CPU time available, other marine radar applications could be incorporated. For instance, algorithms for predicting changes in wind direction and speed could be developed and incorporated. Also, the information reported by the proposed algorithm could be combined with other marine radar software to characterize the current sea state or even to predict sea state changes.

Acknowledgments. We want to thank the Office of Naval Research (ONR) for supporting this research within their Department Research Initiative (DRI) on High-Resolution Air–Sea Interaction (Hi-Res) under Award N00101411WX20493.

REFERENCES

- Bell, P. S., 1999: Shallow water bathymetry derived from an analysis of X-band marine radar images of waves. *Coast. Eng.*, **37**, 513–527.
- Brase, C. H., and C. P. Brase, 2009: *Understandable Statistics: Concepts and Methods*. 3rd ed. Cengage Learning, 798 pp.
- Chaudhry, A., and R. Moore, 1984: Tower-based backscatter measurements of the sea. *IEEE J. Oceanic Eng.*, **9**, 309–316.
- Dankert, H., and W. Rosenthal, 2004: Ocean surface determination from X-band radar-image sequences. *J. Geophys. Res.*, **109**, C04016, doi:10.1029/2003JC002130.

- , and J. Horstmann, 2007: A marine radar wind sensor. *J. Atmos. Oceanic Technol.*, **24**, 1629–1642.
- , —, S. Lehner, and W. Rosenthal, 2003a: Detection of wave groups in SAR images and radar image sequences. *IEEE Trans. Geosci. Remote Sens.*, **41**, 1437–1446, doi:10.1109/TGRS.2003.811815.
- , —, and W. Rosenthal, 2003b: Ocean wind fields retrieved from radar-image sequences. *J. Geophys. Res.*, **108**, 3352, doi:10.1029/2003JC002056.
- Drobinski, P., and R. C. Foster, 2003: On the origin of near-surface streaks in the neutrally-stratified planetary boundary layer. *Bound.-Layer Meteor.*, **108**, 247–256.
- Flampouris, S., F. Ziemer, and J. Seemann, 2008: Accuracy of bathymetric assessment by locally analyzing radar ocean wave imagery (February 2008). *IEEE Trans. Geosci. Remote Sens.*, **46**, 2906–2913, doi:10.1109/TGRS.2008.919687.
- Golub, G. H., and C. F. Van Loan, 1980: An analysis of the total least squares problem. *SIAM J. Numer. Anal.*, **17**, 883–893.
- Lee, P., and Coauthors, 1995: X-band microwave backscattering from ocean waves. *J. Geophys. Res.*, **100** (C2), 2591–2611.
- McWilliams, J., P. Sullivan, and C. Moeng, 1997: Langmuir turbulence in the ocean. *J. Fluid Mech.*, **334**, 1–30.
- Nieto-Borge, J. C., G. Rodríguez, K. Hessner, and P. González, 2004: Inversion of marine radar images for surface wave analysis. *J. Atmos. Oceanic Technol.*, **21**, 1291–1300.
- Senet, C., J. Seemann, and F. Ziemer, 2001: The near-surface current velocity determined from image sequences of the sea surface. *IEEE Trans. Geosci. Remote Sens.*, **39**, 492–505, doi:10.1109/36.911108.
- Trizna, D. B., 1997: A model for Brewster angle damping and multipath effects on the microwave radar sea echo at low grazing angles. *IEEE Trans. Geosci. Remote Sens.*, **35**, 1232–1244.
- , 2010: Method and apparatus for coherent marine radar measurements of properties of ocean waves and currents. U.S. Patent 2010/0315284 A1, filed 26 August 2010.
- , and D. Carlson, 1996: Studies of dual polarized low grazing angle radar sea scatter in nearshore regions. *IEEE Trans. Geosci. Remote Sens.*, **34**, 747–757, doi:10.1109/36.499754.
- Vicen-Bueno, R., R. Carrasco-Alvarez, M. Rosa-Zurera, and J. C. Nieto-Borge, 2009: Sea clutter reduction and target enhancement by neural networks in a marine radar system. *Sensors*, **9**, 1913–1936.
- , —, M. P. Jarabo-Amores, J. C. Nieto-Borge, and E. Alexandre-Cortizo, 2011a: Detection of ships in marine environments by square integration mode and multilayer perceptrons. *IEEE Trans. Instrum. Meas.*, **60**, 712–724.
- , —, —, —, and M. Rosa-Zurera, 2011b: Ship detection by different data selection templates and multilayer perceptrons from incoherent maritime radar data. *IET Radar Sonar Navig.*, **5**, 144–154.
- Young, I., W. Rosenthal, and F. Ziemer, 1985: A three-dimensional analysis of marine radar images for the determination of ocean wave directionality and surface currents. *J. Geophys. Res.*, **90** (C1), 1049–1059.